Rock and Soil Mechanics

Volume 44 | Issue 1 Article 2

3-13-2023

Strength characteristics and mechanism analysis of fiber reinforced highly cohesive tailings solidified using high-calcium geopolymer

Yuan LI
IRSM-CAS/HK Poly. Univ. Joint Laboratory on Solid Waste Science, Wuhan, Hubei 430071, China

Ming-li WEI
Jiangsu Institute of Zoneco Co., Ltd., Yixing, Jiangsu 214200, China

Lei LIU
Wuhan CAS-ITRI Solid Waste Resources Co., Ltd., Wuhan, Hubei 430070, China, lliu@whrsm.ac.cn

Wei WEI
University of Chinese Academy of Sciences, Beijing 100049, China

See next page for additional authors

Custom Citation

LI Yuan, WEI Ming-li, LIU Lei, WEI Wei , CHEN Yi-jun, . Strength characteristics and mechanism analysis of fiber reinforced highly cohesive tailings solidified using high-calcium geopolymer[J]. Rock and Soil Mechanics, 2023, 44(1): 43-53.

Strength characteristics and mechanism analysis of fiber reinforced highly cohesive tailings solidified using high-calcium geopolymer

Authors

Yuan LI, Ming-li WEI, Lei LIU, Wei WEI, and Yi-jun CHEN

Rock and Soil Mechanics 2023 44(1): 43−53 ISSN 1000−7598
https: //doi.org/10.16285/j.rsm.2022.5252 rocksoilmech.researchcommons.org/journal

Strength characteristics and mechanism analysis of fiber reinforced highly cohesive tailings solidified using high-calcium geopolymer

LI Yuan[1, 2,3, 4], WEI Ming-li[1, 3, 5], LIU Lei[1, 3,4,6], WEI Wei[1, 2], CHEN Yi-jun[1, 3, 6]

1. State Key Laboratory of Geomechanics and Geotechnical Engineering, Institute of Rock and Soil Mechanics, Chinese Academy of Sciences, Wuhan, Hubei 430071, China
2. University of Chinese Academy of Sciences, Beijing 100049, China
3. Hubei Province Key Laboratory of Contaminated Sludge and Soil Science and Engineering, Institute of Rock and Soil Mechanics, Chinese Academy of Sciences, Wuhan, Hubei 430071, China
4. IRSM-CAS/HK Poly. Univ. Joint Laboratory on Solid Waste Science, Wuhan, Hubei 430071, China
5. Jiangsu Institute of Zoneco Co., Ltd., Yixing, Jiangsu 214200, China
6. Wuhan CAS-ITRI Solid Waste Resources Co., Ltd., Wuhan, Hubei 430070, China

Abstract: Solidification treatment of highly cohesive tailings is one of the important means for resource utilization. Highly cohesive iron tailings were taken as the object to carry out strength characteristic experiments of solidified tailings using high-calcium geopolymer to analyze the impacts of different dosages of chopped basalt fiber and dry-wet cycles. The micro-cementation behavior, unconfined compressive strength, and the response parameters after dry-wet cycles (strength, mass loss, and electrochemical properties) of the fiber-reinforced solidified materials were discussed. It is concluded that: 1) Adding fiber increased the strength. 0.5% was the optimal dosage (strength increased by 29.1%), which is equivalent to reducing the dosage of geopolymer by about 2%. 2) Fiber, hydration products and tailings were bonded by cementation and frictional occlusion. An appropriate amount of fiber could reduce pore connectivity and increase the capillary water holding capacity. 3) The dry-wet cycles destroyed the cementation, and the damage was stable after the sixth cycle. The fiber has no obvious advantage in improving the dry-wet durability of the solidified materials. The above results provide theoretical support and method reference for clarifying the strength characteristics and durability of solidified tailings.

Keywords: highly cohesive iron tailings; chopped basalt fiber; high-calcium geopolymer; micro-cementation behavior; dry-wet cycles

1 Introduction

The annual output of tailings in China has reached 1.649 billion tons, of which iron tailings are the solid waste generated after the refining of iron ore resources, accounting for 51% of the annual output of tailings[1]. The comprehensive utilization rate of tailings in China is only 18.9% in 2020–2021[1], and it is urgent to improve the resourceful reuse of iron tailings. With the rapid development of advanced beneficiation and ball milling processes, the iron tailings produced have an increasingly high content of clay particles and silt particles, and the strong water-holding and high cohesive properties lead to poor drainage of the tailings agglomerates, making it difficult to solidify them. This is not only detrimental to the safe and efficient operation of the stockpile area, but also increases the difficulty of solidifying the tailings for reuse as engineering fill.

Currently, researchers are mostly using geopolymers as an alternative to cement-based materials for solid waste disposal, which can reduce carbon emissions from cement production (6%–7% of global carbon emissions[2]). Tian et al.[3] solidified tailings of gold ore by excitation of fly ash at 10% by mass with sodium hydroxide to improve the strength of the tailings; Wan et al. [4], on the other hand, constructed a geopolymer of sodium silicate-metakaolin system for curing/stabilizing zinc tailings to improve strength and reduce leaching of zinc contaminants. Sedira et al.[5] used granulated blast furnace slag as a precursor to cure tungsten ore waste with a variety of alkaline solutions (e.g., sodium silicate, sodium hydroxide, potassium hydroxide, sodium hydroxide solution with spent glass powder) for activation. As described in the literature[2−5], the currently developed geopolymer materials are mainly alkali-activated “wo-part” materials[6]. The “two-part” geopolymer is difficult to apply on a large scale due to its high cost, harsh alkali excitation environment and high construction hazards. “One-part” geopolymers can solve these problems by directly mixing the compound with water to form a cementitious strength, like the construction process of cement materials[7−8]. The current research on “one-part” geopolymers is based on the use of solid commercial sodium alkali metal materials, which are costly and do not meet the requirements of a low-carbon economy.

Received: 4 March 2022 Accepted: 2 April 2022
This work was supported by the Special Fund for Basic Research on Scientific Instruments of the National Natural Science Foundation of China (51827814); the Major Science and Technology Project of Inner Mongolia Autonomous Region (No. E139320101) and the Foundation for Distinguished Young Scholars of Hubei Province (2021CFA096).
First author: LI Yuan, male, born in 1996, PhD candidate, focusing on environmental geotechnical engineering. E-mail: liyuan18@mails.ucas.ac.cn
Corresponding author: LIU Lei, male, born in 1982, PhD, Professor, research interests: safe disposal of solid waste. E-mail: lliu@whrsm.ac.cn

The strength of the solidified materials determines the extent to which they can be reused in engineering, while the dry-wet durability of the solidified materials is tested by the rainfall and groundwater scouring that it often faces in service. The addition of fibrous materials can improve the strength and durability of the geopolymer. By comparing the main properties of representative fibers (Table 1), it is found that basalt fibers produced from stable igneous minerals have the advantages of high strength, high modulus, corrosion resistance, oxidation resistance, low thermal conductivity, high compressive and shear strength[9], and are significantly superior to chemical and plant-based fibers such as polypropylene fibers. Wang et al.[10] pointed out that basalt fiber cemented soil has greater dynamic elastic modulus values and higher strength performance than polypropylene fiber cement. In addition, basalt fiber is an environmentally-friendly inorganic fiber. However, few studies have been reported concerning the coupling of basalt fiber with geopolymer for curing iron tailing sand.

This paper focuses on the curing effect of a "one-part" compound-activated high-calcium geopolymer from the effects of basalt fiber admixture and dry-wet cycles on the strength of solidified tailings. Firstly, the unconfined compressive strength of the solidified materials was tested, and the mechanism of strength evolution of the basalt fiber-reinforced solidified materials was discussed in conjunction with thermogravimetric analysis (TGA) and scanning electron microscope pattern (SEM). Secondly, the strength performance, mass loss and electrochemical properties (pH, redox potential ORP, electrical conductivity EC) of the solidified tailings after dry-wet cycles were analyzed to determine the resistance of the solidified tailings to dry-wet cycles after fibrous reinforcement. This study may provide a new idea for the low-carbon curing treatment of high-cohesion tailings.

Table 1 Main performance parameters of representative fibers[8-9, 11−13]

Fiber type	Density /(g·cm^{-3})	Tensile strength /MPa	Elastic modulus /GPa	Melting point /℃	Ultimate elongation /%
Basalt fiber	2.6	3.0×10^3−4.5×10^3	9.5×10^1−1.2×10^2	1.2×10^3	2.4−3.0
Polypropylene fibers	0.9	2.2×10^2−3.4×10^2	3.8	1.6×10^2−1.7×10^2	3.0×10^1−5.0×10^1
Wollastonite fiber	2.8	2.7×10^3−4.1×10^3	3.0×10^2−5.3×10^2	1.5×10^3	—
Straw fiber	0.5	7.0×10^1	1.1	—	1.5
Date palm fiber	1.3	2.8×10^1−2.0×10^2	6.0	—	5.0～1.0×10^1

2 Materials and methods

2.1 Test material

The physical and chemical properties of the highly cohesive iron tailing studied in this paper, which was taken from a stockpile in Lianyungang, are listed in Table 2. The natural moisture content of this tailing was maintained at about 20%, and the plasticity index was 14.7. Referring to the *Standard for geotechnical testing method* (GB/T 50123−2019)[14], the tailings have good particle gradation ($C_u > 5$, $1 < C_c < 3$); and can be classified as clayey sand in accordance with the *Standard for engineering classification of soil* (GB/T 50145−2007)[15]. However, due to its high liquid and plastic limits, great large plasticity index, and the obvious and tight agglomeration of the particles (see Fig.1), it can be classified into a low liquid-limit clay if the engineering classification is based on the plasticity index.

In order to improve the strength of the solidified tailings and the overall utilization of solid waste, we developed a "one-part" composite excitation of high-calcium geopolymer (A alkaline, S slag, F fly ash, abbreviated as ASF) based on industrial waste with the high calcium content. The specific components of ASF included granulated blast furnace slag (grade S95, white powder), fly ash (grey-black powder), metakaolin (fineness 0.050 mm, light pink powder), gypsum (white powder), sodium hydroxide (guaranteed reagent, solid bead), and calcium carbide slag (60% of particles less than 0.075 mm size, white powder). Industrial slags such as slag, fly ash, and metakaolin were precursors for ASF geopolymers and had good potential to be excited. Gypsum was used as a calcium supplement to form a high-calcium system. The solid sodium hydroxide and calcium carbide slag acted as alkaline excitants to improve the excitation efficiency, and the calcium content of the system was supplemented by the calcium carbide slag. The ASF geopolymer did not exceed the standard for heavy metals and other contaminants in each waste fraction.

Table 2 Physicochemical properties of highly cohesive iron tailings

Natural moisture content /%	Relative density	Liquid limit w_L /%	Plastic limit w_P /%	Plasticity index I_P	pH (solid-to-liquid ratio 1:1)	Particle size distribution /%			Uniformity coefficient C_u	Curvature coefficient C_c	Main chemical composition /%				
						Clay particles (<0.005 mm)	Silt particles (0.005−0.075 mm)	Sand particles (0.075−2 mm)			SiO_2	Fe_2O_3	CaO	MgO	Al_2O_3
19.6	2.7	31.2	16.5	14.7	9.4	6.8	19.4	73.8	39.1	0.45	35.5	18.3	12.4	21.4	5.5

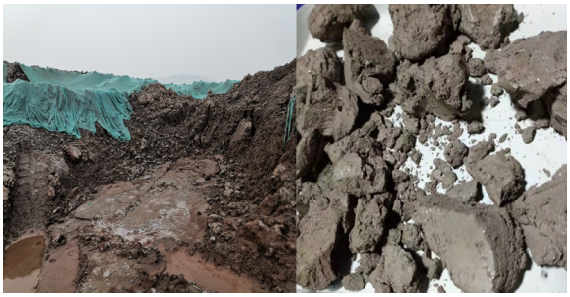

(a) In-situ stockpiling and macro-aggregation of highly cohesive tailing

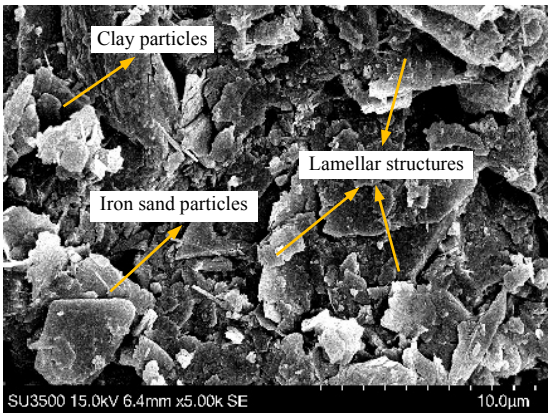

(b) SEM image of a highly viscous tailing sand

Fig. 1 Macro-micro characterization diagrams of raw highly cohesive iron tailings

When the ASF geopolymer is compounded with a solid exciter containing sodium and calcium, its calcium ions, as well as calcium ions from precursors and calcium supplements, can replace the sodium ions in the three-dimensional reticular polymeric gel structure, resulting in the transformation from a hydrated sodium silicate aluminate gel to a hydrated calcium silicate aluminate gel. Compared with the traditional geopolymer system, ASF geopolymer has good pore-filling ability, denser structure, high cementation strength, and also has acid and alkali resistance, low permeability, low shrinkage, and low swelling characteristics[16]. In addition, the ASF geopolymer developed in this paper can significantly reduce the amount of commercial alkali metal exciter dosed, reduce construction hazards and costs, and enable direct mixing and maintenance of the composite ASF material and highly cohesive tailing to build strength.

The reinforcing material used in the test was 3 mm long basalt fiber supplied by a company in Liupanshui, Guizhou province. The components in the ASF geopolymer and the morphology of the basalt fiber are illustrated in Fig.2. The main chemical compositions and contents of the precursors in the ASF geopolymer and basalt fiber were measured by an X-ray fluorescence spectrometer (Shimadzu), as shown in Table 3.

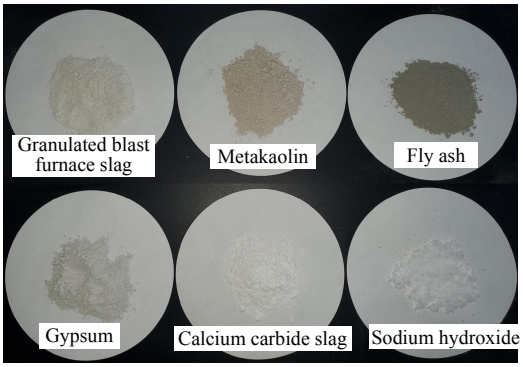

(a) Components of ASF geopolymers

(b) 3 mm basalt fiber

Fig. 2 Photographs of each composition of ASF geopolymer and basalt fiber

Table 3 Main chemical composition and content of ASF geopolymer precursor and basalt fiber

Component	Content /%						
	SiO_2	Al_2O_3	CaO	Fe_2O_3	MgO	Na_2O	K_2O
Slag	30.8	14.8	41.1	0.3	8.5	—	0.5
Fly ash	49.5	35.0	4.8	4.7	0.5	—	1.3
Metakaolin	52.2	44.0	0.3	0.7	0.3	0.2	0.7
Basalt fiber	32.7	13.7	10.2	19.9	5.0	7.5	—

2.2 Test methodology

2.2.1 Specimen preparation and curing

The application process for ASF geopolymer and basalt fiber is shown in Fig.3. The specimen preparation process was developed for both indoor testing and on-site engineering implementation. The components are pre-mixed dry and homogeneous until the color of the mixture is consistent; the fiber is uniformly distributed and then mixed with high cohesion tailing, pressed into shape, and cured. The natural moisture content of the tailing provides a good water environment for the ASF geopolymer reaction without the need for additional rehydration.

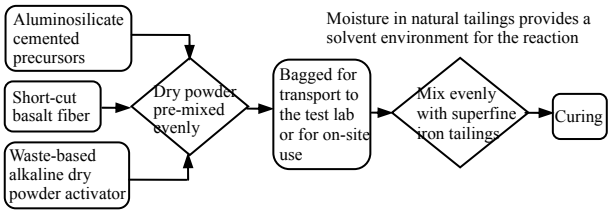

Fig. 3 Specimen preparation process of tailings solidified by geopolymer and basalt fiber

The sample preparation process referred to *Test methods of materials stabilized with inorganic binders for highway engineering* (JTG E51－2009)[17] and *Standard for geotechnical testing method* (GB/T 50123－2019)[14]. The specimen size was set at 50 mm× 50 mm, and the mixture was hydrostatically pressed into the sample in one step. The cured iron tailings with 3% and 5% ASF dosages (accounting for a percentage of the dry mass of the tailings) were used as the test control group and were recorded as A3F0 and A5F0. Considering the economics of the fiber, the 3% ASF cured masses with 0.2%, 0.5% and 1.0% basalt fibers (accounting for a percentage of the dry mass of the tailings) were studied and were abbreviated as A3F0.2, A3F0.5 and A3F1.0 respectively. The samples were sealed in plastic bags and cured in a standard oven at a humidity of 95% ± 2% and a temperature of 20 ± 1°C.

2.2.2 Test methods

To better investigate the strength characteristics and mechanisms of fiber-reinforced high calcium geopolymer cured high cohesion tailings, the research approach adopted in this paper is shown in Fig. 4. The strength performance of fiber-cured tailings is first investigated, the interface lap behaviors and strength performance mechanisms of the fiber-cured bodies are analyzed through microscopic interaction tests, and finally, the durability of the fiber-cured highly cohesive tailings under the influence of dry-wet cycles is discussed from a strength perspective. In short, this study attempts to answer the question of whether fiber can be used in cured highly cohesive tailings from an application perspective and how they perform in terms of dry-wet durability during service.

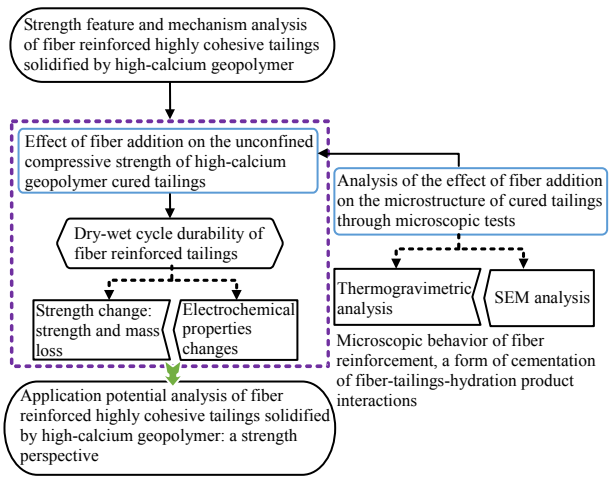

Fig. 4 Flow chart of research idea in this study

Based on the research idea, the design scheme for the object, age and number of specimens maintained in this test is shown in Table 4, and the specific test methods are described in (1) to (3) below.

(1) Unconfined compressive strength test

The unconfined compressive strength test was carried out according to ASTM D4219－08[18], The sample preparation process referred to *Test methods of materials stabilized with inorganic binders for highway engineering* (JTG E51－2009)[17] and *Standard for geotechnical testing method* (GB/T 50123－2019)[14]. The test equipment was a digital display hydraulic-type pressure tester (Jinan Chenda Testing Machine Manufacturing Co., Ltd.) with a controlled axial strain rate of 1 %/min.

Table 4 Experimental design scheme

Test classification	Test item	Studied object	Curing time	Number of samples
Conventional strength tests	Unconfined compressive strength	A3F0, A3F0.2, A3F0.5, A3F1.0, A5F0	7, 14, 28 d	3 per age
Microscopic test	TGA test	A3F0, A3F0.2, A3F0.5, A3F1.0	28 d	1 per studied object
	SEM test	A3F0, A3F0.5, A3F1.0	7, 28 d	1 per age and per study subject (A3F0 after 7 d of curing only)
Dry-wet durability test	Unconfined compressive strength	A3F0, A3F0.2, A3F0.5, A3F1.0	2, 4, 6, 8 cycles	3 per cycle and per studied object
	Strength control group	A3F0, A3F0.2, A3F0.5, A3F1.0	20, 26, 32, 38 d	3 per age and per studied object
	Mass loss	A3F0, A3F0.2, A3F0.5, A3F1.0	8 cycles	1 per cycle and per studied object
	Electrochemical parameters	A3F0, A3F0.2, A3F0.5, A3F1.0	0, 2, 4, 6, 8 cycles	1 group of debris per cycle and per studied object

(2) Micro-mechanism tests

The hydration of the sample needs to be stopped before the microscopic test. The specimens were first placed in a 100 mL plastic, anhydrous ethanol was poured into container. The specimens were soaked for 1 d, and then were removed and placed in a vacuum drying oven and dried at 50 °C for 48 h. After the termination of hydration, the specimens were subjected to SEM and TGA tests.

The SEM test was carried out using a LEO1530VP instrument manufactured by American FEI Company. The TGA test was carried out using a TGA/DSC 2 instrument from METTLER TOLEDO, Switzerland, with a temperature range of 30−800 °C and a temperature rise rate of 10 °C/min.

(3) Dry-wet cycle test

After 14 d of curing, the specimens were subjected to a dry-wet cycle test, as described in the literature [16]. The dry cycle lasted 48 h at 50 ± 1 °C. After the dry cycle, the specimens were soaked in deionized water and transferred to a standard oven for the wet cycle (20 ± 1 °C), which lasted 24 h. This was one dry-wet cycle test. The entire dry-wet cycle test was

carried out for a total of 8 cycles. After each dry-wet cycle, the mass of the specimens was measured, the mass loss rate was calculated, and the unconfined compressive strength was tested after 0, 2, 4, 6, and 8 dry-wet cycles. During the dry-wet cycle, the control group continued to be maintained conventionally. After reaching the corresponding curing time, the specimens in the control group were removed and tested together for strength together with the dry-wet tested specimens described above.

The soaking solution used in the wet cycle was Milli-Q deionized water, prepared on an instrument by Merck Millipore, Germany.

The electrochemical tests were carried out by collecting dry-wet specimens after strength tests subjected to 0, 2, 4, 6, and 8 dry-wet cycles, including pH, electrical conductivity (EC) and oxidation-reduction potential (ORP). The specific test method is described in the literature [19−20]. 20 g of debris was placed in a centrifuge tube, 20 mL of deionized water was added, and the tube was sealed and placed in a horizontal shaker at 20 ± 1 °C for 1 h. After 1 h, the tube was removed and centrifuged at 3 000 r/min for 5 min. The supernatant was taken to test the electrochemical parameters. The pH was measured with the Inlab Routine Pro electrode, the ORP with the Inlab Redox Electrode and the EC with the InLab710 Electrode from METTLER TOLEDO Switzerland. The electrodes were connected to the METTLER TOLEDO FE28 benchtop mainframe to display the data.

3 Result and discussion

3.1 Strength evolution

Figure 5 compares the strength of A3F0, A3F0.2, A3F0.5, A3F1.0 and A5F0 after 7, 14 and 28 d of curing. It can be found that:

(1) The unconfined compressive strength increased with age. The strength of most specimens varied with age. For A3F0 specimens, the 14 d and 28 d strengths increased by 6.77% and 49.2%, respectively as compared to the 7 d strength; the A3F1.0 strengths increased by 28.3% and 51.3%, respectively.

(2) Fiber reinforcement increased the unconfined compressive strength. The unconfined compressive strength of A3F0 was approximately 0.89 MPa after 7 d of curing. The unconfined compressive strength was increased by 16.5%, 29.1% and 24.2% when 0.2%, 0.5% and 1.0% of fiber were incorporated, respectively. For 28 d of curing, the strength was increased by 6.94%, 19.1% and 26.0%, respectively.

(3) The amount of fiber incorporated did not increase as much as possible. After 7 d of curing, the 0.2% and 1.0% fiber doses had a poorer effect on strength than the 0.5% fiber dose. Among the solidified materials, A3F0.5 had the highest strength at 14 d of curing at approximately 1.75 MPa.

The strength of A3F0.5 after 14 d and 28 d of curing was similar to the strength of A3F1.0 and A5F0 after 28 d of curing. The strength of A3F0.5 after 28 d of curing was slightly lower than that of A3F1.0 after 28 d of curing, but the increase in strength at 28 d from 0.2% to 0.5% (approx. 12.2%) was higher than the increase in strength from 0.5% to 1.0% (approx. 7%). Furthermore, the amount of fiber and curing agent used should be kept as low as possible in terms of economy. Therefore, a 0.5% dose of basalt fiber is the optimum dose, especially for the early strength of the solidified materials. The incorporation of 0.5% fiber reduces the amount of fiber by approx. 0.5% or the amount of curing agent by approx. 2.0%.

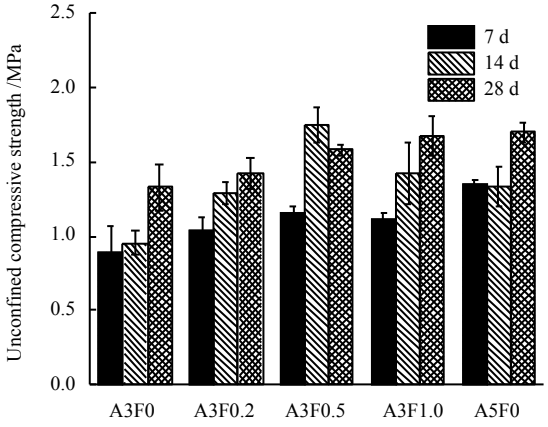

Fig. 5 Impact of basalt fiber dosage on unconfined compressive strength of solidified materials

3.2 Microscopic behavior and mechanisms

3.2.1 Thermogravimetric analysis

Figure 6(a) shows the TG curves of the basalt fiber-reinforced solidified materials, with the temperature of 500 °C being the cut-off point. The mass loss of A3F0 before 500 °C was greater than that of the fiber-reinforced solidified materials. The mass loss from 30 to 300 °C was mainly attributed to the evaporation and dehydration process of free water and chemically bound water in the hydration products inside the specimen at high temperatures[21]. The addition of fiber will increase the water retention of solidified materials and can adsorb water molecules after the destruction of bound water; therefore, the solidified materials with fiber incorporating had the lowest mass loss rate. A3F0.2 had a strong water retention capacity in the range of 30 to 300 °C, especially for the strongly adsorbed water that changed after 120 °C. It indicated that a small amount of fiber incorporation will fill part of the pores and produce a small amount of hydrated gel in small pores, thus reducing pore connectivity. In turn, the existence of micro-pores composed between these particles increases a certain capillary water-holding capacity. The increase in fibers tends to link the capillary pores to form larger interconnected pores,

and the fibers themselves are repulsive, resulting in the solidified materials and fibers having a lower water holding capacity and increasing the interfacial contact gap between the fiber-hydration product and the tailings[22]. The cumulative mass loss rate of A3F0 at 500 °C was approximately 1.91%. After 500 °C, the mass loss rate of the fiber-added solidified materials was gradually greater than that of A3F0 as the temperature increased, and this phenomenon was more obvious after 600°C. The high temperature causes the destruction of the hydration products and the decomposition of calcite ($CaCO_3$) in tailings; the presence and decomposition of $CaCO_3$ are illustrated by the strong peak in the derivative thermogravimetric (DTG) curve at around 700°C in Fig.6(b), which ultimately results in a rapid loss of mass[23−24]. The different melting points of the fiber-hydration product-tailings mixtures[25], as well as the agglomeration phenomenon of the fibers, cause uncoordinated strains at the fiber cementation interface under high temperature or erosive environments, resulting in more mass loss due to more exposure of the surfaces of the tailings hydration products to high temperatures[26].

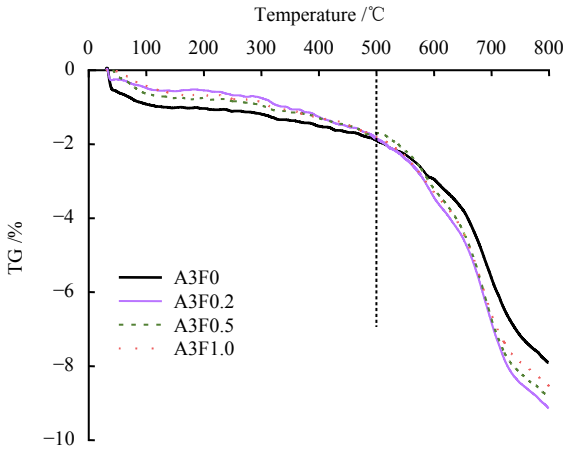

(a) Thermogravimetric (TG) change curve

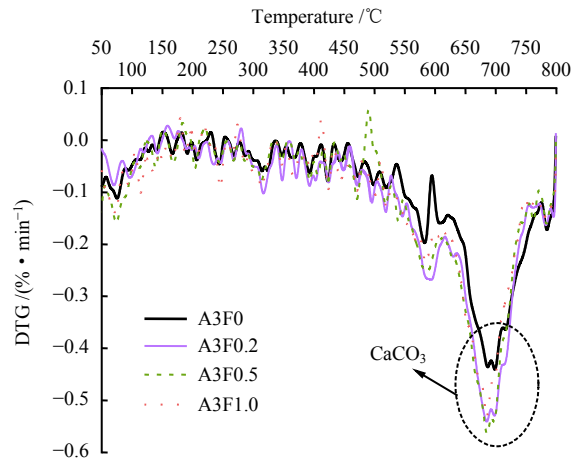

(b) Derivative thermogravimetric (DTG) change curve

Fig. 6 Thermogravimetric analysis of basalt fiber reinforced solidified materials after 28 d curing

3.2.2 Scanning electron microscope analysis

Figure 7 presents an SEM image of A3F0 after 7 d of curing, showing the complete hydration product−tailings cementation interface. At a curing agent of 3%, the hydration products were less, and the filling effect was poorer. Due to the short curing age, the reaction is not sufficient, and the fly ash activity is low, so there is still a large amount of fly ash spherical vitreous structure that has not yet participated in the reaction [27]. As the age of curing increases, the fly ash breaks down, and further silicate and aluminate monomers are released, which are further hydrated with the calcium ions in the solution. This explains the significant increase in strength (28 d) in the later stages of A3F0.

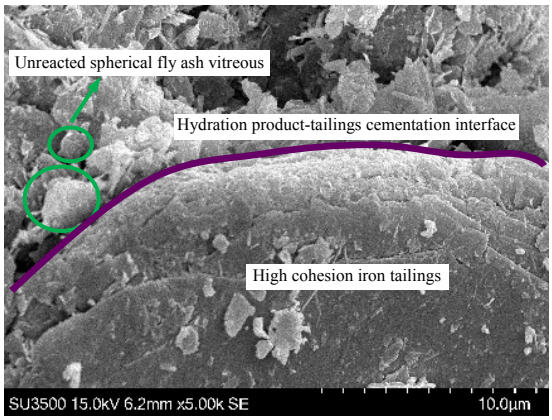

Fig. 7 Scanning electron microscopy of A3F0 solidified materials after 7 d curing

The strength of the solidified materials increased with increasing admixture (0.2%, 0.5%) and did not necessarily increase significantly at higher dosage (1.0%). The fiber reinforcement effect was further analyzed by SEM images of typical fiber-reinforced solidified materials (A3F0.5 and A3F1.0) after 7 d and 28 d of curing (Figs. 8 and 9). The images show that the fibers are scattered in single or clustered form within the solidified materials, fitting closely to the tailings and hydration products to form a whole.

As shown in Figs. 8(a) and 8(b), A3F0.5 and A3F1.0 can be combined in clusters in the solidified materials, and the outer surface of the clustered fiber fitted closely with the hydration products and tailings, forming a cementing interface, which was also adsorbed and combined with a small amount of hydration products on the surface of the clustered fiber, with a certain cementing and bonding ability; when the fiber incorporation was higher (Fig.8(b)), the arrangement between the fibers was more disordered, which had some adverse effect on the strength. When the image was magnified (Figs. 8(c) and 8(d)), it was observed that the binding state of the individual fibers was more tightly cemented and wrapped by the hydration products and the tailings. As the curing age increased (Fig.9), a large amount of cementation products were produced in the solidified materials after 28 d of hydration, which encapsulated the fibers more tightly, making the fibers−hydration

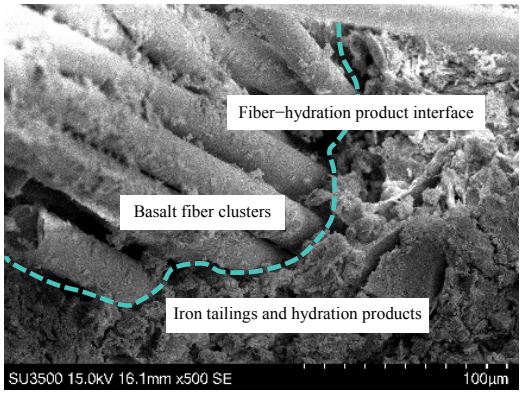

(a) A3F0.5 (100 μm scale)

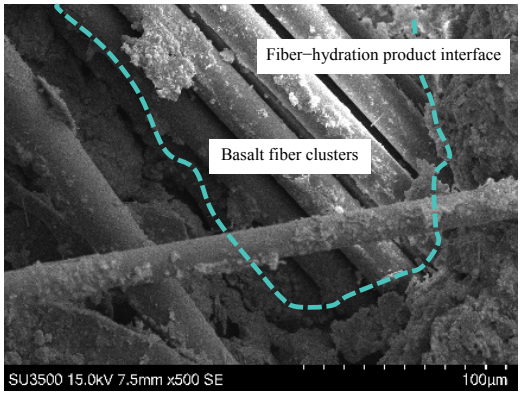

(b) A3F1.0 (100 μm scale)

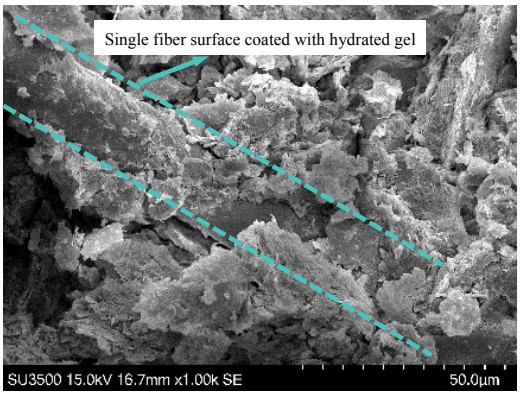

(c) A3F0.5 (50 μm scale)

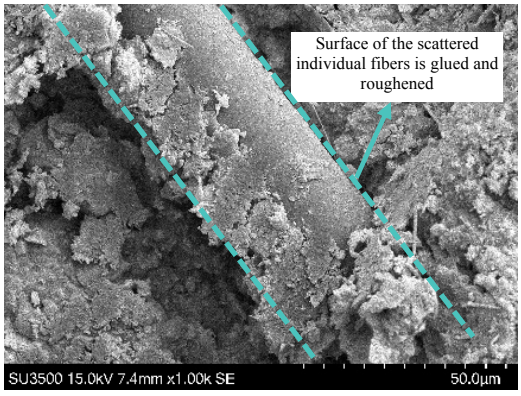

(d) A3F1.0 (50 μm scale)

Fig. 8 Microscopic morphology of chopped basalt fibers in A3F0.5 and A3F1.0 after 7 d of curing

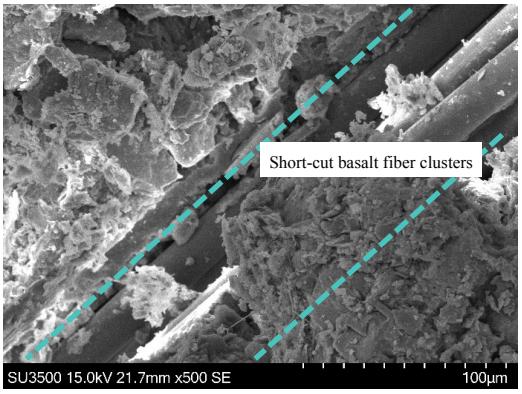

(a) A3F0.5 (100 μm scale)

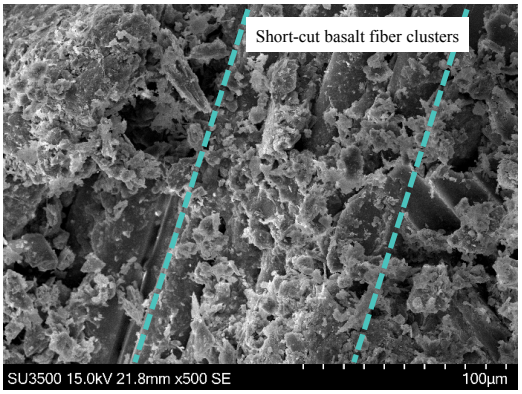

(b) A3F1.0 (100 μm scale)

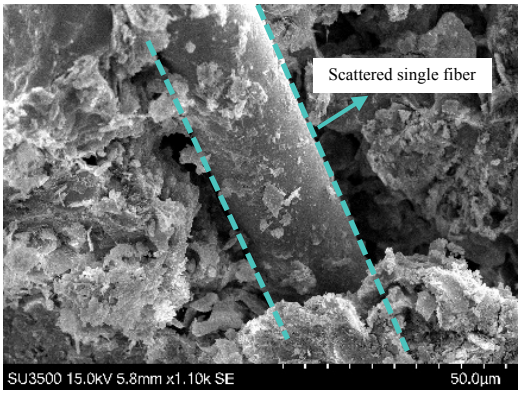

(c) A3F0.5 (50 μm scale)

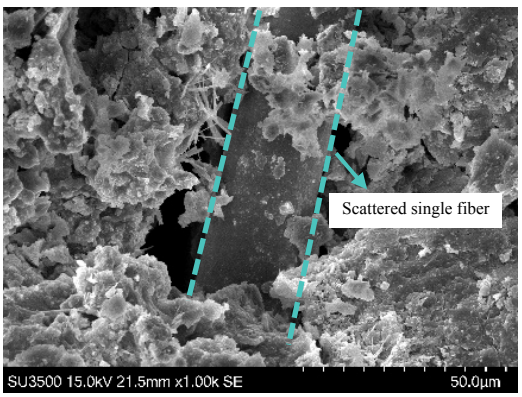

(d) A3F1.0 (50 μm scale)

Fig. 9 Microscopic morphology of chopped basalt fibers in A3F0.5 and A3F1.0 after 28 d of curing

products−tailings form a denser whole and increasing the strength. Figure 9(b) shows that the large amount of hydration products wrapped around the clustered fibers resulted in a more regular fiber arrangement and denser bonding in A3F1.0 compared to the 7 d curing, as a result, a slightly higher strength than that of A3F0.5. Figures 9(c) and 9(d) illustrate that the hydration products were more abundant, but detailed observations revealed that the cementation of the fiber−hydration products was still weak and that hydrolysis, damage and even fracture may occur preferentially along this interface when the solidified materials were damaged by dry-wet cycle induced erosion.

The interfacial contact of the fiber−tailings−hydration products is cementation and frictional occlusion[28], and the concept of this interfacial contact mechanism can be seen in Fig.10. Due to the different properties of the various substances in the mixture, when the force and deformation of the fiber, tailings and hydration products are not coordinated, it will affect the interfacial forces on the cementation interface so that the solidified materials are prone to shear damage at the interface bond. Under the action of cementation and friction, the right amount of fiber can restrain the deformation of the tailings and provide higher shear strength than the tailing particles, which causes higher strength growth by bearing part of the force for the curing body. However, excessive dosage may cause a disorderly arrangement of fibers, affecting the filling effect of hydration products. With the increasing age of curing, a large amount of hydration gel products are generated, which can also improve the mechanical relationship of the interface. This effect is more reflected in the increased ability of the hydration products to wrap fibers and tailings, increasing the cementation and frictional occlusion of fiber−hydration product−tailings[29]. Specifically, the original surface of the basalt fibers is relatively smooth, and the hydration gel wrapped around them can improve the frictional effect of the fibers. It is important to emphasize that there are still some ungelled voids at the fiber−hydration product interface.

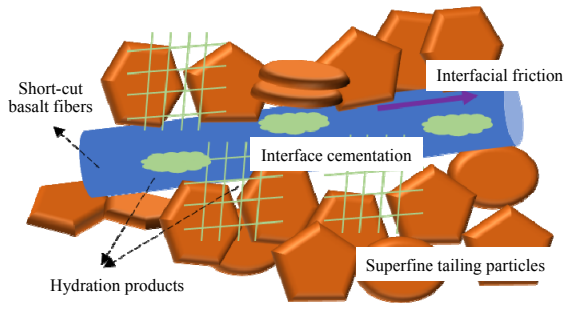

Fig. 10 Conceptual model of interface interaction between basalt fiber, highly cohesive tailings, and hydration products

3.3 Effect of dry-wet cycles

3.3.1 Strength change and mass loss rate

Figure 11 presents the pattern of change in the unconfined compressive strength of specimens after dry-wet cycles. The specimens in the control group were not subjected to dry-wet cycles and were conventionally cured. Compared to conventional curing (Fig.11(a)), Fig.11(b) shows that the dry-wet cycles significantly weakened the strength of the solidified materials. Comparing the strengths after 0, 2, 4, 6, and 8 cycles, meaning 14, 20, 26, 32, and 38 d, it was found that the strength of the individual solidified materials decreased rapidly in the first 2 cycles tests and then fluctuated and increased slightly as the number of cycles increased. In the early stages of dry-wet cycles, the destruction of solidified materials prevailed, i.e., rapid destruction of the skeletal structure; in the middle and late stages of dry-wet cycles, the dry-wet cycles induced damage reached stability, with the formation of some secondary products and even a slight increase in strength[30]. The strengths of A3F0, A3F0.2, A3F0.5 and A3F1.0 were 0.95, 0.92, 0.97 and 0.99 MPa when subjected to 8 cycles, with little difference in strength between the individual solidified materials after a total of 8 dry-wet cycles. In addition, a comparison of the strength of the solidified materials without dry-wet cycles (Fig.11(a))

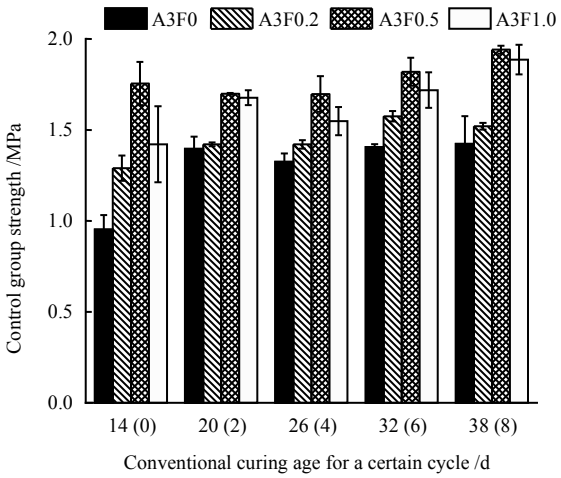

(a) Strength of the solidified materials after conventional curing age corresponding to the number of dry-wet cycles

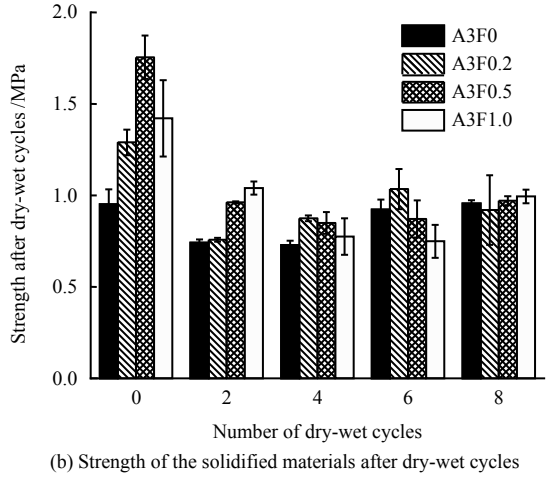

(b) Strength of the solidified materials after dry-wet cycles

Fig. 11 Unconfined compressive strength of highly cohesive tailings solidified materials after dry-wet cycles and control strength

showed that the strength of the fiber-reinforced solidified materials was significantly reduced, and the presence of fibers affected the long-term durability of the solidified materials. The effect of different fiber dosing levels on the dry-wet cycle durability of the solidified materials was not significant, and the advantages of fiber adding were not obvious.

Figure 12 shows the rate of mass change of solidified materials with different doses of basalt fiber after various dry-wet cycles. The mass of each solidified material tended to decrease as the number of dry-wet cycles increased. The mass loss rate of each solidified material was basically stable after 6 cycles, with a total loss rate ranging from 2% to 3%. A3F0.2 and A3F0.5 had a slightly lower total loss rate, demonstrating that the appropriate amount of fiber adding had a restraining effect and reduced particle stripping. However, the mass loss paths of the solidified materials differed slightly during the cycle. A3F0 and A3F1.0 showed a large variation in the loss rate during the first 6 cycles, especially in the first 2 cycles, while A3F0.2 and A3F0.5 showed a uniform decrease in mass loss rate during the first 6 cycles.

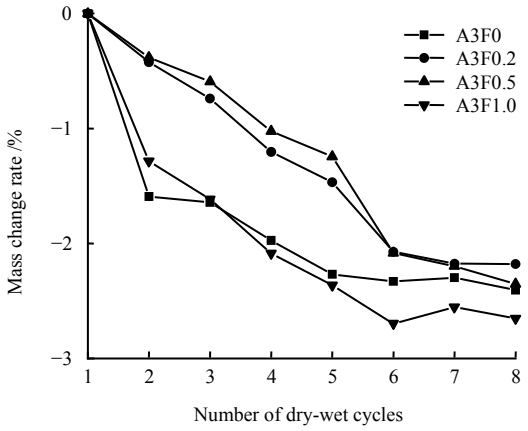

Fig. 12 Mass change rate of solidified materials with the increase of dry-wet cycles

The SEM pattern revealed that the surface of the basalt fiber was relatively smooth, and its interface with the solidified materials was mainly based on the cementation and frictional occlusion between the fiber−hydration products and the tailings particles. The cementation was mainly the development and covering of the hydration products, while the frictional occlusion could also roughen the fiber surface through the hydration products, which in turn exhibited some overall frictional effect. In a long-term dry-wet cyclic erosive environment, the interfacial bonding pattern in the fiber solidified materials gradually weakened as the hydration products gradually decreased. During the early stages of long-term erosion, the fibers still had some restraining and reinforcing effect, but the hydration products were significantly reduced as erosion increased, resulting in more exposure to the smoother surfaces of the fibers. And the erosion solution can erode the inside of solidified materials through the voids created by fiber−hydration product−tailings damage, which makes its resistance to erosion insignificant.

3.3.2 Changes in electrochemical parameters

The changes in pH, EC and ORP values of the solidified materials after dry-wet cycles at cycles of 0, 2, 4, 6 and 8 are shown in Fig.13. Figure 13(a) shows that the pH of all specimens decreased significantly after erosion of 8 dry-wet cycles and that the adding of fiber promoted a reduction in the pH of the solidified materials, which contributed to a reduction in the degree of environmental contamination from the alkaline leachate of the solidified materials during service. When the number of dry-wet cycles increased from 0 to 8, the pH of A3F0.2 decreased from 11.12 to 9.25, A3F0.5 from 11.26 to 9.15, A3F1.0 from 10.99 to 9.34, and A3F0 from 11.15 to 9.50. Meanwhile, the dry-wet cycles reduced the pH of the specimen and also stalled the hydration reaction of the solidified materials, which increased the destruction of the hydration products[31]. The gradual stabilization of the pH change after 6 dry-wet cycles reflected the fact that erosion damage reached damage equilibrium. The destruction of hydration products and surface erosion of fibers and tailings can be reflected by the EC values, as shown in Fig.13(b). In the first 2 levels of wet-dry cycles, the damage of the solidified materials was more severe and a large number of ions leached out, resulting in higher EC values, which was consistent with the results of strength loss in early stage of dry-wet cycles. The EC values of the individual solidified materials were stable and not significantly different after 6 cycles, indicating that the degree of damage was similar across the solidified materials and that the fiber incorporation did not significantly improve the dry-wet resistance of the solidified materials. The change in ORP values shown in Fig. 13(c) reflected the chemical reaction of the solidified materials[32]. The ORP value of the solidified materials after adding fiber was higher, particularly A3F0.2 and A3F0.5. Combining with the data on the reduction in strength after dry-wet cycles, it indicated that the fiber adding promoted the occurrence of decomposition and destruction reactions of the hydration products to some extent, causing a significant reduction in strength of the fiber-reinforced solidified materials after dry-wet erosion. The ORP value of the solidified materials was relatively stable and decreased slightly after 6 cycles, indicating that the erosion damage had reached stability at this point.

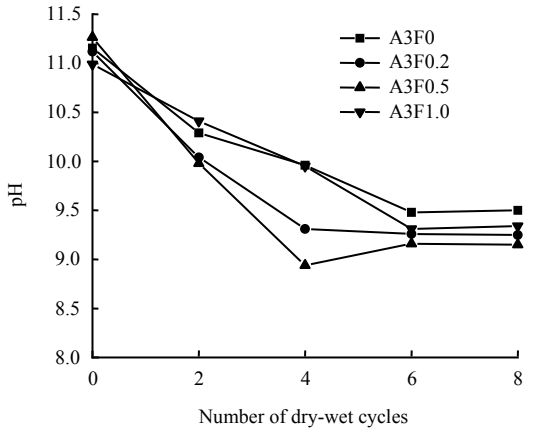

(a) pH change

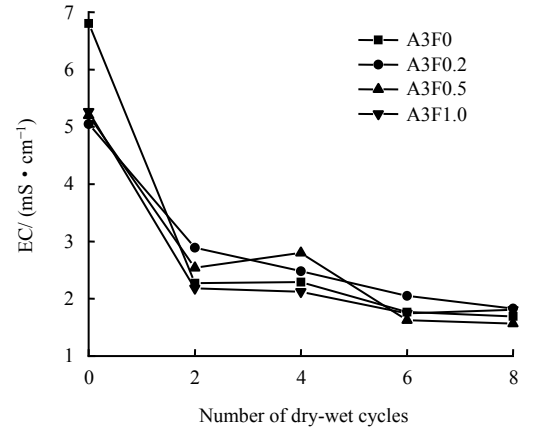

(b) Changes in electric conductivity (EC)

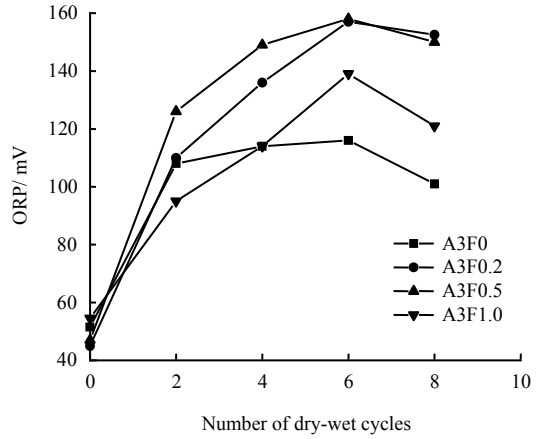

(c) Changes in oxidation-reduction potential (ORP)

Fig. 13 Changes of typical electrochemical properties of solidified materials after dry-wet cycles

4 Conclusion

This paper investigated the mechanism of the effect of basalt fiber incorporation and dry-wet cycles on the strength of highly cohesive tailings cured by high calcium geopolymer. The main conclusions are drawn as follows:

(1) In terms of unconfined compressive strength, the addition of basalt fibers increase the strength. The A3F0.5 specimen has the highest strength at 14 d, approximately 1.75 MPa, indicating that 0.5% is the optimum dosage. Moreover, the long-term strength of A3F0.5 is close to that of A5F0, and the 0.5% fiber reduced the amount of curing agent by approximately 2%.

(2) In terms of microscopic cementation, single or clustered basalt fibers are dispersed in the solidified materials, and the interface of fiber−tailings−hydration products is cemented and frictionally occluded. In addition, the proper amount of fibers can restrain the deformation of the tailings, fill the pores, and also partially withstand the forces for the cured tailings in case of damage.

(3) In terms of dry-wet cycles, the first 2 levels of cycles are more intense, and the damage reaches equilibrium and stability after 6 cycles. The strength of each solidified material does not differ significantly after the complete cycle, with a relatively large reduction in the strength of the fiber-reinforced solidified material. The advantage of fiber adding after the dry-wet cycles is not significant.

References

[1] GU Xiao-wei, AI Ying-ying, ZHAO Yun-qi, et al. Status quo of resource utilization of iron ore tailings[J/OL]. The Chinese Journal of Nonferrous Metals, 2022: 1-29 (2022-02-15) [2022-01-13]. https://kns.cnki.net/kcms/detail/43.1238.TG.20220112.1844.002.html.

[2] AMRAN Y H M, ALYOUSEF R, ALABDULJABBAR H, et al. Clean production and properties of geopolymer concrete; a review[J]. Journal of Cleaner Production, 2020, 251: 119679.

[3] TIAN X, ZHANG H, ZHANG T, et al. Alkali-activated copper tailings-based pastes: compressive strength and microstructural characterization[J]. Journal of Materials Research and Technology, 2020, 9(3): 6557−6567.

[4] WAN Q, RAO F, SONG S, et al. Immobilization forms of ZnO in the solidification/stabilization (S/S) of a zinc mine tailing through geopolymerization[J]. Journal of Materials Research and Technology, 2019, 8(6): 5728−5735.

[5] SEDIRA N, CASTRO-GOMES J. Effect of activators on hybrid alkaline binder based on tungsten mining waste and ground granulated blast furnace slag[J]. Construction and Building Materials, 2020, 232: 117176.

[6] KALISZ S, KIBORT K, MIODUSKA J, et al. Waste management in the mining industry of metals ores, coal, oil and natural gas-a review[J]. Journal of Environmental Management, 2021, 304: 114239.

[7] MA C, ZHAO B, GUO S, et al. Properties and characterization of green one-part geopolymer activated by composite activators[J]. Journal of Cleaner Production, 2019, 220: 188−199.

[8] ABDOLLAHNEJAD Z, MASTALI M, WOOF B, et al. High strength fiber reinforced one-part alkali activated

slag/fly ash binders with ceramic aggregates: microscopic analysis, mechanical properties, drying shrinkage, and freeze-thaw resistance[J]. Construction and Building Materials, 2020, 241: 118129.

[9] RALEGAONKAR R, GAVALI H, ASWATH P, et al. Application of chopped basalt fibers in reinforced mortar: a review[J]. Construction and Building Materials, 2018, 164: 589−602.

[10] WANG Min-min, LU Qun, GUO Shao-long, et al. Dynamic behavior of soil with fiber and cement under cyclic loading[J]. Rock and Soil Mechanics, 2018, 39(5): 1753−1760.

[11] GUO L, WU Y, XU F, et al. Sulfate resistance of hybrid fiber reinforced Metakaolin geopolymer composites[J]. Composites Part B: Engineering, 2020, 183: 107689.

[12] NAIR N A, SAIRAM V. Research initiatives on the influence of wollastonite in cement-based construction material−a review[J]. Journal of Cleaner Production, 2021, 283: 124665.

[13] SUPIAN A B M, JAWAID M, RASHID B, et al. Mechanical and physical performance of date palm/ bamboo fiber reinforced epoxy hybrid composites[J]. Journal of Materials Research and Technology, 2021, 15: 1330−1341.

[14] Ministry of Water Resources of the People's Republic of China. GB/T 50123－2019 Standard for geotechnical testing method[S]. Beijing: China Planning Press, 2019.

[15] Ministry of Water Resources of the People's Republic of China. GB/T 50145－2007 Standard for engineering classification of soil[S]. Beijing: China Planning Press, 2008.

[16] WEI M, LI Y, YU B, et al. Low-carbon treatment of zinc contaminated iron tailings using high-calcium geopolymer: influence of wet-dry cycle coupled with acid attack[J]. Journal of Cleaner Production, 2022, 338: 130636.

[17] Institute of Highway Science, Ministry of Communications. JTG E51－2009 Test method of materials stabilized with inorganic binders for highway engineering[S]. Beijing: China Communications Press, 2009.

[18] American Society for Testing Material. D4219－08 Standard test method for unconfined compressive strength index of chemical-grouted soils[S]. West Conshohocken: ASTM International, 2008.

[19] LI Y, WEI M, LIU L, et al. Adsorption of toluene on various natural soils: influences of soil properties, mechanisms, and model[J]. Science of the Total Environment, 2020, 740: 140104.

[20] WEI M, LI Y, YU B, et al. Assessment of semi-dynamic leaching characteristics of lead and zinc from stabilized contaminated soil using sustainable phosphate-based binder after carbonation[J]. Journal of Cleaner Production, 2022, 332: 130126.

[21] AHMAD M R, CHEN B. Microstructural characterization of basalt fiber reinforced magnesium phosphate cement supplemented by silica fume[J]. Construction and Building Materials, 2020, 237: 117795.

[22] NIU D, SU L, LUO Y, et al. Experimental study on mechanical properties and durability of basalt fiber reinforced coral aggregate concrete[J]. Construction and Building Materials, 2020, 237: 117628.

[23] WANG L, CHO D W, TSANG D C W, et al. Green remediation of As and Pb contaminated soil using cement-free clay-based stabilization/solidification[J]. Environment International, 2019, 126: 336−345.

[24] WANG L, CHEN L, TSANG D C W, et al. Mechanistic insights into red mud, blast furnace slag, or metakaolin-assisted stabilization/solidification of arsenic-contaminated sediment[J]. Environment International, 2019, 133(Pt B): 105247.

[25] ŞAHIN F, UYSAL M, CANPOLAT O, et al. Effect of basalt fiber on metakaolin-based geopolymer mortars containing rilem, basalt and recycled waste concrete aggregates[J]. Construction and Building Materials, 2021, 301: 124113.

[26] ALASKAR A, ALBIDAH A, ALQARNI A S, et al. Performance evaluation of high-strength concrete reinforced with basalt fibers exposed to elevated temperatures[J]. Journal of Building Engineering, 2021, 35: 102108.

[27] SHAH K W, HUSEIEN G F. Bond strength performance of ceramic, fly ash and GBFS ternary wastes combined alkali-activated mortars exposed to aggressive environments[J]. Construction and Building Materials, 2020, 251: 119088.

[28] WANG D, WANG H, LARSSON S, et al. Effect of basalt fiber inclusion on the mechanical properties and microstructure of cement-solidified kaolinite[J]. Construction and Building Materials, 2020, 241: 118085.

[29] WANG S, XUE Q, MA W, et al. Experimental study on mechanical properties of fiber-reinforced and geopolymer-stabilized clay soil[J]. Construction and Building Materials, 2021, 272: 121914.

[30] GAO H, LIAO L, LIANG Y, et al. Improvement of durability of porous perlite geopolymer-based thermal insulation material under hot and humid environment [J]. Construction and Building Materials, 2021, 313: 125417.

[31] WEI M, NI H, ZHOU S, et al. Feasibility of stabilized Zn and Pb contaminated soils as roadway subgrade materials[J]. Advances in Materials Science and Engineering, 2020, 2020: 1025056.

[32] LV Y, XIAO K, YANG J, et al. Correlation between oxidation-reduction potential values and sludge dewaterability during pre-oxidation[J]. Water Research, 2019, 155: 96−105.